Title: Live cell reporters reveal bidirectional acceleration of nucleocytoplasmic transport by O-GlcNAc modification of the nuclear pore complex

Authors: Tae Yeon Yoo, Timothy J Mitchison

Affiliation: Department of Systems Biology, Blavatnik Institute, Harvard Medical School, Boston, MA 02115, USA.

Abstract: Macromolecular transport across the nuclear envelope is fundamental to eukaryotic cells and depends on facilitated diffusion through nuclear pore complexes (NPCs). The interior of NPCs contains a permeability barrier made of phenylalanine-glycine (FG) repeat domains that selectively facilitates the permeation of cargoes bound to nuclear transport receptors (NTRs)[1,2]. The NPC is enriched in O-linked N-acetylglucosamine (O-GlcNAc) modification[3-8], but its functional role in nucleocytoplasmic transport is unclear. We developed high-throughput assays based on optogenetic probes to quantify the kinetics of nuclear import and export in living human cells and showed that the O-GlcNAc modification of the NPC accelerates the nucleocytoplasmic transport in both directions. Super-resolution imaging of O-GlcNAc revealed strong enrichment at the FG barrier of the NPC channel. O-GlcNAc modification also promoted the passive permeation of a small, inert protein through NPCs. Our results suggest that O-GlcNAc modification accelerates nucleocytoplasmic transport by enhancing the non-specific permeability the FG-repeat barrier.

Main text

Nucleocytoplasmic transport occurs through nuclear pore complexes (NPCs) built from nucleoporins (NUPs), many of which are FG-NUPs that project disordered regions containing phenylalanine-glycine (FG) repeats into the central channel to constitute a selective permeability barrier[1,2]. FG-NUPs are heavily modified by O-linked β-N-acetylglucosamine (O-GlcNAc)[3-6] reversibly attached to the hydroxyl oxygen of serine and threonine. Previous *in vitro* studies have shown that O-GlcNAcylation alters the structure and permeability of hydrogels derived from

FG domains[9] as well as the radius of gyration of FG domains in solution[10]. These observations in a simplified biochemical model system predict that O-GlcNAcylation might increase the permeability of NPCs and promote nucleocytoplasmic transport in living cells, but this has never been tested, in large part due to the absence of quantitative tools to measure transport rates in cells. Here, we overcome this limitation using optogenetics. Alteration of nucleocytoplasmic transport has been implicated in many physiological and pathological processes[11-13], so tools to measure and perturb it will find multiple uses. In cells, O-GlcNAcylation was proposed to affect NPC integrity and composition[14,15]. This predicts a change in NPC density following O-GlcNAc perturbation, which we also tested.

To quantify nuclear import and export kinetics we repurposed the NES-mCherry-LINuS and NLS-mCherry-LEXY probes previously created for light-controlled gene expression[16,17]. They consist of LINuS (LOV2-based photoactivatable NLS)[16] and LEXY (LOV2-based photoactivatable NES)[17] attached to mCherry along with a constitutive NES or NLS that counteracts the photoactivatable signals (Fig. 1a, b). The NES-mCherry-LINuS import probe is mostly localized in the cytoplasm in the dark state but translocates to the nucleus upon blue-light stimulation as the activated LINuS overpowers the NES (Fig. 1a). Likewise, the NLS-mCherry-LEXY export probe translocates mostly from the nucleus to the cytoplasm upon blue-light stimulation (Fig. 1b). The kinetics of light-induced changes in the nuclear intensity of the probes were well-described by mono-exponential decay models. This allowed accurate fitting of kinetic data to output single decay constants which report transport rates. The light-induced conformational change of LOV2 is so fast[18] that it does not contribute to the overall translocation kinetics. The dark-reversibility of LINuS and LEXY allows repeated measurements of the transport rates in individual cells. We generated U2OS cell lines stably expressing the transport probes and automated image acquisitions and analysis to allow high-throughput, time-course measurement and accurate detection of rate changes with high statistical confidence (Fig. 1c).

To validate the transport assays, we quantified the effects of known perturbations. We first tested the effects of siRNA-mediated depletions of the following NUPs: Nup96-Nup98 precursor, Nup153, Nup214, and Tpr (Fig. 1d,

Extended Data Table 1). Different NUP depletions differentially affected the import/export kinetics of the LINuS/LEXY probes: Nup96/98 and Nup153 depletions resulted in the largest reduction in the import rate of the LINuS probe (~60%), followed by Nup214 (39%) and Tpr (27%) depletions. The export rate of the LEXY probe was also greatly affected by Nup96/98 and Nup153 depletions (~30%), while slightly by Tpr and Nup214 depletions (~6%). These findings demonstrate the capability of the transport assays to separately measure the differential changes in the import and export rates induced by different perturbations (Supplementary Discussion).

We next tested the effect of nuclear transport inhibitors. We first inhibited nuclear import by expressing bimax2, a peptide that competitively inactivates importin-αs by tightly binding to their NLS-binding domains[19]. We found that the import rate of the LINuS probe sharply decreased with an increasing GFP-bimax2 expression level, while GFP expression alone did not affect the rate (Fig. 1e). We next inhibited the nuclear export using KPT-330, a specific inhibitor of exportin-1, an NTR accommodating diverse NESs[20,21]. After KPT-330 treatment, the export rate of the LEXY probe decreased by 75% (Fig. 1f). The import rate of the LINuS probe also decreased by 62% after KPT-330 treatment, but the relative reduction of the export rate to that of the import rate nonetheless was much greater for KPT-330 treatment than those for NUP depletions (Extended Data Fig. 1, Extended Data Table 1). These results demonstrate that the LINuS and LEXY probes quantitatively report on the importin-α/β1-dependent import and the exportin-1-dependent export rates, respectively, although they are not fully decoupled (Supplementary Discussion).

With quantitative assays in hand, we investigated how nuclear transport rates respond to perturbation of O-GlcNAc modifications. We first performed siRNA transfections to deplete O-GlcNAc transferase (OGT) or O-GlcNAcase (OGA), the sole pair of enzymes that add and remove O-GlcNAc[8]. After 3 days of the siRNA transfections, we found that the import rate was 45% lower in the OGT-depleted cells, while 11% higher in the OGA-depleted cells, compared to cells transfected with scrambled siRNA (Fig. 2a). The export rate followed the same trend as the import rate but changed to smaller extents (Fig. 2a). Consequently, the import and export rates

were about 100% and 30% higher, respectively, in the OGA-depleted cells than in the OGT-depleted cells (Extended Data Table 1).

We next used OGT- or OGA-specific small-molecule inhibitors, OSMI-4[22] and Thiamet-G[23], respectively, to better control the timing and degree of the OGT/OGA inhibitions. Cells were treated with each drug at three different doses and continually assayed for the nuclear transport rates over 20 hours. The import rate slightly decreased (7%) in the DMSO control over the time of on-stage incubation. It decreased significantly more in the presence of OSMI-4 in a dose-dependent manner, by up to 23% over 20 hours (Fig. 2b). The decay rate measured $0.14 \pm 0.02\ h^{-1}$, comparable to the turnover rate of O-GlcNAc at several NUPs measured previously[24]. On the other hand, the import rate increased after Thiamet-G treatment in a dose-dependent manner up to 15% over 20 hours (Fig. 2b). Similarly, the nuclear export rate also reached a higher and lower level in the presence of Thiamet-G and OSMI-4, respectively, than in the DMSO control (Fig. 2b).

To characterize the relationship between the O-GlcNAc level and the transport rates, we performed quantitative immunofluorescence using RL2, anti-O-GlcNAc antibody generated against glycosylated NUPs[6]. Compared to the DMSO control, the nuclear RL2 signal decreased by up to 52% in the OSMI-4-treated cells and increased by up to 30% in the Thiamet-G-treated cells, exhibiting dose dependency in both directions (Fig. 2c). Plotting the transport rates (shown in Fig. 2b) against the nuclear RL2 signals (shown in Fig. 2c) revealed that both transport rates increased linearly with increasing nuclear RL2 signal, with the import rate showing a greater dependency (Fig. 2d). The relationship between the import and export rates measured after the drug-induced OGT/OGA inhibitions was colinear with that after OGT/OGA RNAi, indicating that the O-GlcNAc-dependent change in the rates is independent of the mechanism of perturbation (Extended Data Fig. 1).

We further asked whether the O-GlcNAc dependency of the transport rates was specifically due to modification of NPCs where O-GlcNAc is abundant[3-6], as opposed to less direct effects mediated by changes in gene expression[25] or modification of other factors in the transport machinery[2]. Hypothetically, if the NPCs or other nucleus-confined

components were responsible for the O-GlcNAc-dependent transport rates, different nuclei in a multi-nucleated cell could have different transport rates depending on their O-GlcNAc levels. To test this, we generated heterokaryons using polyethylene glycol (PEG)-mediated cell fusion[26] (Fig. 3a). Briefly, two U2OS stable cell lines, one expressing GFP-labeled histone 2A (GFP-H2A) and the other expressing the NES-mCherry-LINuS import probe, were separately transfected with OGT- or OGA-targeting siRNA. Then those two cell populations were combined and treated briefly with PEG to induce cell fusion (Fig. 3a). The multi-nucleated cells were assayed after 2-4 hours of resting in the presence of both OSMI-4 and Thiamet-G to suppress O-GlcNAc turnover. This maintained pre-fusion levels of O-GlcNAcylation in each nucleus after fusion (Fig. 3b).

We performed cell fusions with every combination of the two siRNA transfections (OGT or OGA) and the two cell lines (GFP-H2A or NES-mCherry-LINuS) and measured the nuclear import rate of the GFP+ nuclei in mCherry+ cells (Fig. 3a,c). The GFP positivity indicates the origin of the nucleus and therefore its O-GlcNAc state, while the mCherry positivity ensures the fusion with the other origin. The siOGT/siOGT or siOGA/siOGA fusions displayed similar import rates to the OGT- and OGA-depleted unfused cells, respectively, indicating that the cell fusion itself does not alter the transport rates (Fig. 3c). Interestingly, in the siOGT/siOGA heterokaryons, the import rate was 28% higher at the high-O-GlcNAc nuclei than at the low-O-GlcNAc nuclei (Fig. 3c), indicating a significant contribution of the nucleus-confined factors to the O-GlcNAc-dependent nuclear transport regulation.

We next asked which nuclear transport machinery components are responsible for the O-GlcNAc dependency of nuclear import observed in the cell fusion assay. The NPC itself is undoubtedly the top qualified candidate not only for the abundance of O-GlcNAc modification[3-6] but also for its strict confinement to the nucleus[27,28]. The strict nuclear confinement was confirmed by heterokaryon fusion analyses: Nup96 was not exchanged between the nuclei in a heterokaryon, neither was Nup153, despite its dynamic association with the NPC[27,28] (Extended Data Fig. 2). We also considered the possibility that the Ran pathway plays a role in the O-GlcNAc dependency of the import rate, as Rcc1 and RanGAP1, the two major regulators of Ran, are confined to the nucleus at least

partially[29-31]. However, OSMI-4 or Thiamet-G treatment did not result in any appreciable change in the distributions of Ran, Rcc1, and RanGAP1 (Extended Data Fig. 3). More importantly, the nuclear/cytoplasmic ratio of RanGTP level, measured by anti-RanGTP antibody[32] immunostaining, was not affected by the O-GlcNAc perturbations, but by the overexpression of WT or mutant Ran (Ran^{Q69L} and Ran^{T24N}) or Rcc1, which confirms the validity of the RanGTP immunoassay (Extended Data Fig. 3). Thus, the O-GlcNAc-dependent regulation of nuclear transport rate is predominantly driven by the NPCs, rather than by the Ran-regulating system or other diffusive components of the transport machinery, such as NTRs or cargos.

To gain insight into how O-GlcNAcylation alters the NPC, we investigated the distribution of O-GlcNAc within the NPC. Previous studies showed that wheat germ agglutinin (WGA), a GlcNAc-binding lectin, is predominantly localized to the center of the NPC[33,34]. However, WGA may misrepresent the O-GlcNAc distribution due to its multiple binding sites and considerable size (36 kDa)[35]. Moreover, the O-GlcNAc distribution along the transport axis has not been revealed. We therefore employed the combination of metabolic labeling approach and copper(I)-catalyzed azide-alkyne cycloaddition (CuAAC) reaction[36] to fluorescently label O-GlcNAc sites *in situ* and performed super-resolution microscopy (Fig. 4a, b). To set reference points within the NPC, Nup96 was labeled with Alexa Fluor 647 via CRISPR-Cas9-mediated endogenous protein tagging and direct immunostaining using a single-domain antibody (Fig. 4c). We first imaged the double-stained cells using three-dimensional structured-illumination microscopy (3D-SIM) and confirmed a remarkably high level of O-GlcNAc at the NPCs (Fig. 4d, Extended Data Fig. 4). We next used stochastic reconstruction microscopy (STORM) to obtain the detailed O-GlcNAc distribution within the NPC. Viewed from the top, Nup96 delineated the circular periphery of the NPC whose diameter measured 96 ± 8 nm (s.d.) (Fig. 4e, f, Extended Data Fig. 4). O-GlcNAc was concentrated the most at the center and lower at the periphery, resembling the binding pattern of WGA[33,34]. In the side view of the NPC, Nup96 was situated along two lines delineating the top and bottom of the symmetric core of the NPC, separated by ~50 nm (Fig. 4g, h, Extended Data Fig. 4). O-GlcNAc was localized mostly between the two lines and symmetrically distributed along the transport axis (Fig. 4g, h, Extended Data Fig. 4). These results show that

O-GlcNAc is particularly abundant within the channel of the symmetric central core of the NPC where the FG repeat permeability barrier is embedded[37].

The permeability of the FG repeat barrier to the NTR-cargo complex is determined by two factors: specific binding of NTR to FG repeats and non-specific interactions between permeants and the FG barrier[2,38,39]. O-GlcNAc modification could alter either. Previous *in vitro* studies did not report any appreciable change of NTR binding to FG domains following change in O-GlcNAcylation[9,10]. Consistent with this observation, we found that the localization of importin-β1 to NPC was unaltered after O-GlcNAc perturbations by OGT/OGA inhibitions (Extended Data Fig. 5). To determine the effect of O-GlcNAc on interactions between permeants and the barrier independent of specific bindings, we measured the transport rate of a protein probe that does not interact specifically with FG repeats. We photoconverted mEOS inside the nucleus and quantified its rate of passive permeation out of the nucleus (Fig. 5a). We found that the passive permeation rate was 22% lower in the OSMI-4-treated cells and 30% faster in the Thiamet-G-treated cells (Fig. 5a). These data followed the same trend as NTR-facilitated nuclear transport rates (Fig. 2). Since both facilitated and passive transports are accelerated by O-GlcNAcylation we conclude that it mainly increases non-specific permeation rates.

We next considered the possibility that the change in the rates does not result from the altered per-NPC permeability, but from the change in the number of NPCs, since a previous study suggested that O-GlcNAcylation protects NUPs from proteasomal degradation[14]. However, treating cells with 10 μM OSMI-4 or Thiamet-G for 24 hours did not significantly affect the number or area density of the NPCs, measured by MAb414 immunostaining and 3D-SIM (Fig. 5b, Extended Data Fig. 5). Moreover, recent proteomics data[22] of HEK293T show that the levels of NUPs, as well as other transport machinery components, do not considerably change after 24-hour treatment with 20 μM OSMI-4 (Extended Data Fig. 5). Therefore, O-GlcNAcylation did not regulate NPC stability in our system. Rather, it increased non-specific permeability of the FG barrier, thereby enhancing both facilitated and passive transport in both directions (Fig. 5c). This confirms predictions made using synthetic FG-

repeat-derived hydrogels[9]. The enhanced non-specific permeability might result from the hydrophilic and bulky O-GlcNAc moieties hindering the hydrophobic cohesions of FG domains (Fig. 5c).

In summary, we developed quantitative nuclear transport assays and applied super-resolution microscopy to reveal the role of NPC O-GlcNAcylation in modulating the transport rates. The transport assays allow high-throughput quantification of the nuclear import and export kinetics in live cells, overcoming the limitations of conventional assays that rely on the measurement of the steady-state nuclear/cytoplasmic localization of cargos or on membrane-specific permeabilization of cells. The O-GlcNAc-dependent modulation of the transport rates may underlie the mechanism by which OGA inhibition mitigates the nuclear transport defects in Huntington's disease[11] and may also provide a novel way to treat other neurodegenerative diseases and aging-related stresses compromising the nuclear transport machinery[12,13,40].

Acknowledgements: This study was supported by the NIH/NIGMS research grant R35GM131753 and postdoctoral fellowship F32GM131585. We thank Prof. Suzanne Walker, Dr. Zebulon Levine and George Fei (Harvard Medical School) for providing OSMI-4 and RL2 antibody and advice on O-GlcNAc experiments; Prof. Ian Macara (Vanderbilt University) for providing anti-RanGTP antibody; Dr. Luke Lavis (Janelia Research Campus) for providing Janelia Fluor dyes; and Dr. Yuyu Song (Mass General Hospital) for providing anti-Ran antibody. We also thank the Nikon Imaging Center and Cell Biology Microscopy Facility at Harvard Medical School, especially Dr. Talley Lambert, for help with light microscopy and comments on the data and method section.

Author contributions: T.Y.Y. and T.J.M. conceived the study and wrote the manuscript. T.Y.Y. designed and performed the experiments and analyzed the data with input from T.J.M.

Competing interests: The authors declare no competing interests.

References

1 Beck, M. & Hurt, E. The nuclear pore complex: understanding its function through structural insight. *Nat Rev Mol Cell Biol* **18**, 73-89, doi:10.1038/nrm.2016.147 (2017).

2 Wente, S. R. & Rout, M. P. The nuclear pore complex and nuclear transport. *Cold Spring Harb Perspect Biol* **2**, a000562, doi:10.1101/cshperspect.a000562 (2010).

3 Hanover, J. A., Cohen, C. K., Willingham, M. C. & Park, M. K. O-linked N-acetylglucosamine is attached to proteins of the nuclear pore. Evidence for cytoplasmic and nucleoplasmic glycoproteins. *J Biol Chem* **262**, 9887-9894 (1987).

4 Davis, L. I. & Blobel, G. Nuclear pore complex contains a family of glycoproteins that includes p62: glycosylation through a previously unidentified cellular pathway. *Proc Natl Acad Sci U S A* **84**, 7552-7556, doi:10.1073/pnas.84.21.7552 (1987).

5 Holt, G. D. *et al.* Nuclear pore complex glycoproteins contain cytoplasmically disposed O-linked N-acetylglucosamine. *J Cell Biol* **104**, 1157-1164, doi:10.1083/jcb.104.5.1157 (1987).

6 Snow, C. M., Senior, A. & Gerace, L. Monoclonal antibodies identify a group of nuclear pore complex glycoproteins. *J Cell Biol* **104**, 1143-1156, doi:10.1083/jcb.104.5.1143 (1987).

7 Hart, G. W. Dynamic O-linked glycosylation of nuclear and cytoskeletal proteins. *Annu Rev Biochem* **66**, 315-335, doi:10.1146/annurev.biochem.66.1.315 (1997).

8 Chatham, J. C., Zhang, J. & Wende, A. R. Role of O-Linked N-acetylglucosamine (O-GlcNAc) Protein Modification in Cellular (Patho)Physiology. *Physiol Rev*, doi:10.1152/physrev.00043.2019 (2020).

9 Labokha, A. A. *et al.* Systematic analysis of barrier-forming FG hydrogels from Xenopus nuclear pore complexes. *EMBO J* **32**, 204-218, doi:10.1038/emboj.2012.302 (2013).

10 Tan, P. S. *et al.* Two Differential Binding Mechanisms of FG-Nucleoporins and Nuclear Transport Receptors. *Cell Rep* **22**, 3660-3671, doi:10.1016/j.celrep.2018.03.022 (2018).

11 Grima, J. C. *et al.* Mutant Huntingtin Disrupts the Nuclear Pore Complex. *Neuron* **94**, 93-107 e106, doi:10.1016/j.neuron.2017.03.023 (2017).

12 Kim, H. J. & Taylor, J. P. Lost in Transportation: Nucleocytoplasmic Transport Defects in ALS and Other Neurodegenerative Diseases. *Neuron* **96**, 285-297, doi:10.1016/j.neuron.2017.07.029 (2017).

13 Cho, U. H. & Hetzer, M. W. Nuclear Periphery Takes Center Stage: The Role of Nuclear Pore Complexes in Cell Identity and Aging. *Neuron* **106**, 899-911, doi:10.1016/j.neuron.2020.05.031 (2020).

14 Zhu, Y. *et al.* Post-translational O-GlcNAcylation is essential for nuclear pore integrity and maintenance of the pore selectivity filter. *J Mol Cell Biol* **8**, 2-16, doi:10.1093/jmcb/mjv033 (2016).

15 Mizuguchi-Hata, C., Ogawa, Y., Oka, M. & Yoneda, Y. Quantitative regulation of nuclear pore complex proteins by O-GlcNAcylation. *Biochim Biophys Acta* **1833**, 2682-2689, doi:10.1016/j.bbamcr.2013.06.008 (2013).

16 Niopek, D. *et al.* Engineering light-inducible nuclear localization signals for precise spatiotemporal control of protein dynamics in living cells. *Nat Commun* **5**, 4404, doi:10.1038/ncomms5404 (2014).

17 Niopek, D., Wehler, P., Roensch, J., Eils, R. & Di Ventura, B. Optogenetic control of nuclear protein export. *Nat Commun* **7**, 10624, doi:10.1038/ncomms10624 (2016).

18 Konold, P. E. *et al.* Unfolding of the C-Terminal Jalpha Helix in the LOV2 Photoreceptor Domain Observed by Time-Resolved Vibrational Spectroscopy. *J Phys Chem Lett* **7**, 3472-3476, doi:10.1021/acs.jpclett.6b01484 (2016).

19 Kosugi, S. *et al.* Design of peptide inhibitors for the importin alpha/beta nuclear import pathway by activity-based profiling. *Chem Biol* **15**, 940-949, doi:10.1016/j.chembiol.2008.07.019 (2008).

20 Kirli, K. *et al.* A deep proteomics perspective on CRM1-mediated nuclear export and nucleocytoplasmic partitioning. *Elife* **4**, doi:10.7554/eLife.11466 (2015).

21 Lapalombella, R. *et al.* Selective inhibitors of nuclear export show that CRM1/XPO1 is a target in chronic lymphocytic leukemia. *Blood* **120**, 4621-4634, doi:10.1182/blood-2012-05-429506 (2012).

22 Martin, S. E. S. *et al.* Structure-Based Evolution of Low Nanomolar O-GlcNAc Transferase Inhibitors. *J Am Chem Soc* **140**, 13542-13545, doi:10.1021/jacs.8b07328 (2018).

23 Yuzwa, S. A. *et al.* A potent mechanism-inspired O-GlcNAcase inhibitor that blocks phosphorylation of tau in vivo. *Nat Chem Biol* **4**, 483-490, doi:10.1038/nchembio.96 (2008).

24 Wang, X. *et al.* A Novel Quantitative Mass Spectrometry Platform for Determining Protein O-GlcNAcylation Dynamics. *Mol Cell Proteomics* **15**, 2462-2475, doi:10.1074/mcp.O115.049627 (2016).

25 Comer, F. I. & Hart, G. W. O-GlcNAc and the control of gene expression. *Biochim Biophys Acta* **1473**, 161-171, doi:10.1016/s0304-4165(99)00176-2 (1999).

26 Davidson, R. L. & Gerald, P. S. Improved techniques for the induction of mammalian cell hybridization by polyethylene glycol. *Somatic Cell Genet* **2**, 165-176, doi:10.1007/BF01542629 (1976).

27 Rabut, G., Doye, V. & Ellenberg, J. Mapping the dynamic organization of the nuclear pore complex inside single living cells. *Nat Cell Biol* **6**, 1114-1121, doi:10.1038/ncb1184 (2004).

28 Daigle, N. *et al.* Nuclear pore complexes form immobile networks and have a very low turnover in live mammalian cells. *J Cell Biol* **154**, 71-84, doi:10.1083/jcb.200101089 (2001).

29 Nemergut, M. E. & Macara, I. G. Nuclear import of the ran exchange factor, RCC1, is mediated by at least two distinct mechanisms. *J Cell Biol* **149**, 835-850, doi:10.1083/jcb.149.4.835 (2000).

30 Matunis, M. J., Coutavas, E. & Blobel, G. A novel ubiquitin-like modification modulates the partitioning of the Ran-GTPase-activating protein RanGAP1 between the cytosol and the nuclear pore complex. *J Cell Biol* **135**, 1457-1470, doi:10.1083/jcb.135.6.1457 (1996).

31 Mahajan, R., Delphin, C., Guan, T., Gerace, L. & Melchior, F. A small ubiquitin-related polypeptide involved in targeting RanGAP1 to nuclear pore complex protein RanBP2. *Cell* **88**, 97-107, doi:10.1016/s0092-8674(00)81862-0 (1997).

32 Richards, S. A., Lounsbury, K. M. & Macara, I. G. The C terminus of the nuclear RAN/TC4 GTPase stabilizes the GDP-bound state and mediates interactions with RCC1, RAN-GAP, and HTF9A/RANBP1. *J Biol Chem* **270**, 14405-14411, doi:10.1074/jbc.270.24.14405 (1995).

33 Loschberger, A. *et al.* Super-resolution imaging visualizes the eightfold symmetry of gp210 proteins around the nuclear pore complex and resolves the central channel with nanometer resolution. *J Cell Sci* **125**, 570-575, doi:10.1242/jcs.098822 (2012).

34 Thevathasan, J. V. *et al.* Nuclear pores as versatile reference standards for quantitative superresolution microscopy. *Nat Methods* **16**, 1045-1053, doi:10.1038/s41592-019-0574-9 (2019).

35 Wright, C. S. & Kellogg, G. E. Differences in hydropathic properties of ligand binding at four independent sites in wheat germ agglutinin-oligosaccharide crystal complexes. *Protein Sci* **5**, 1466-1476, doi:10.1002/pro.5560050803 (1996).

36 Boyce, M. *et al.* Metabolic cross-talk allows labeling of O-linked beta-N-acetylglucosamine-modified proteins via the N-acetylgalactosamine salvage pathway. *Proc Natl Acad Sci U S A* **108**, 3141-3146, doi:10.1073/pnas.1010045108 (2011).

37 Lin, D. H. & Hoelz, A. The Structure of the Nuclear Pore Complex (An Update). *Annu Rev Biochem* **88**, 725-783, doi:10.1146/annurev-biochem-062917-011901 (2019).

38 Hulsmann, B. B., Labokha, A. A. & Gorlich, D. The permeability of reconstituted nuclear pores provides direct evidence for the selective phase model. *Cell* **150**, 738-751, doi:10.1016/j.cell.2012.07.019 (2012).

39 Rout, M. P., Aitchison, J. D., Magnasco, M. O. & Chait, B. T. Virtual gating and nuclear transport: the hole picture. *Trends Cell Biol* **13**, 622-628, doi:10.1016/j.tcb.2003.10.007 (2003).

40 Hutten, S. & Dormann, D. Nucleocytoplasmic transport defects in neurodegeneration - Cause or consequence? *Semin Cell Dev Biol*, doi:10.1016/j.semcdb.2019.05.020 (2019).

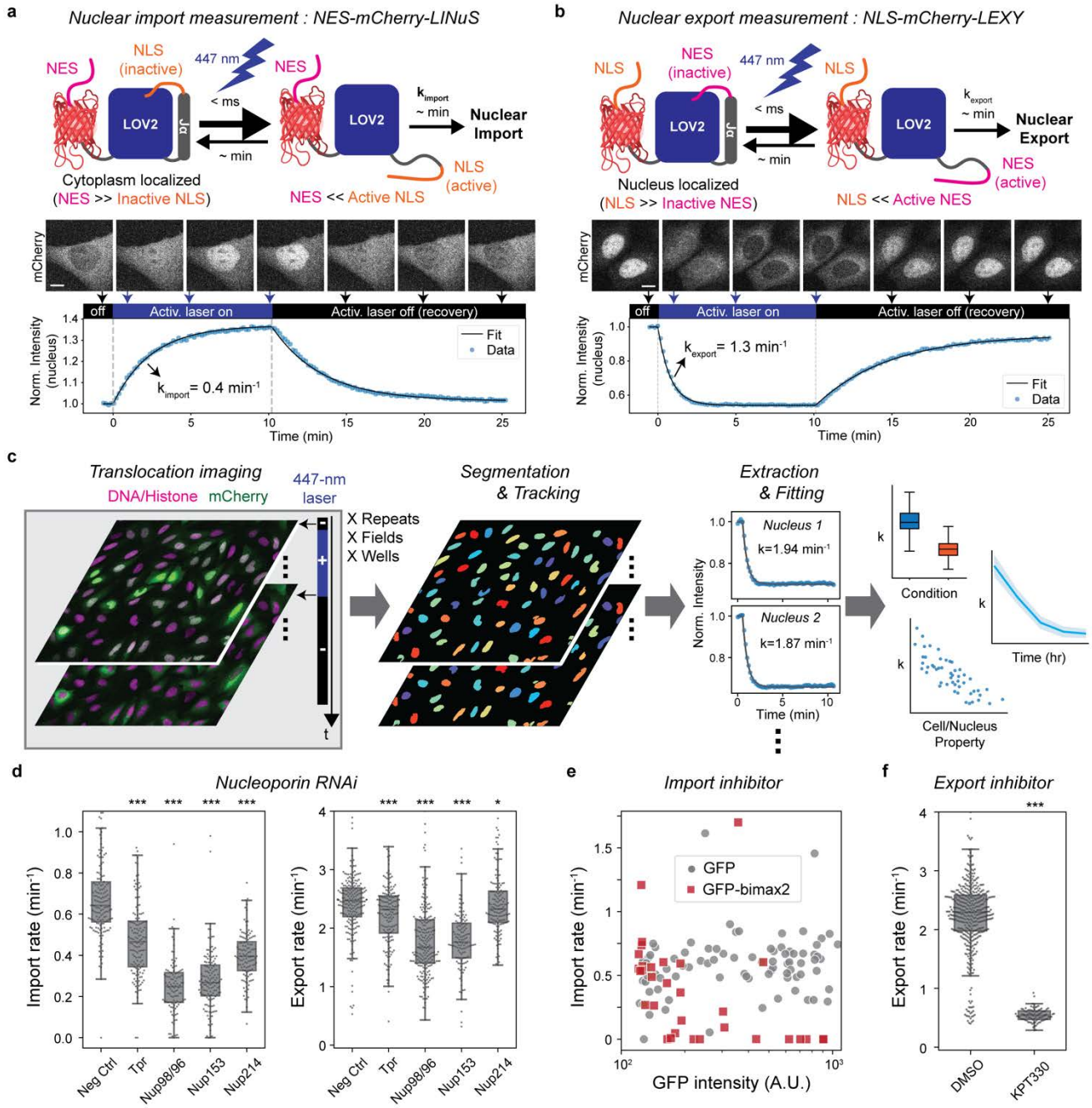

Fig. 1. Development and validation of optogenetics-based live-cell nuclear transport assay. a-b, Measurement of nuclear import and export rates using light-inducible nuclear transport systems, LINuS (import) and LEXY (export). Upon 447-nm laser illumination, NES-mCherry-LINuS and NLS-mCherry-LEXY probes translocate from the cytoplasm to the nucleus and vice versa, respectively. Nuclear transport rates are determined by fitting the light-induced change of the nuclear mCherry intensity to a mono-exponential decay model. When the activation radiation is ceased, the probes return to their pre-illumination locations, allowing repeated measurements. Scale bar, 10 μm. **c**, Automated acquisition and analysis of nuclear transport assay. U2OS cells stably expressing the transport probes and histone-marker are imaged every 10 seconds in the absence and presence of the 447-nm activation laser illumination. The cycle of 10 min activation and 15 min recovery is repeated at multiple locations or time points, if necessary. Nuclei are segmented and tracked based on the histone or DNA images. The time course of the nuclear mCherry intensity was fitted to a mono-exponential decay model to measure the nuclear import or export rate of each nucleus. Measured transport rates were then aggregated for correlation analysis. **d-f**, Validation of the nuclear transport assay by measuring the effects of nuclear transport perturbations. **d**, NUP RNAi, N>100 nuclei for each RNAi condition. **e**, GFP-bimax2 transfection for importin-α sequestration. **f**, 30 min 1 μM KPT-330 treatment for export inhibition. N>90 nuclei. p-values were calculated by Welch's t-test for comparison with negative control. n.s.: p>0.01; *: p<1e-2, **: p<1e-3, ***: p<1e-4. The data is also available in Extended Data Table 1.

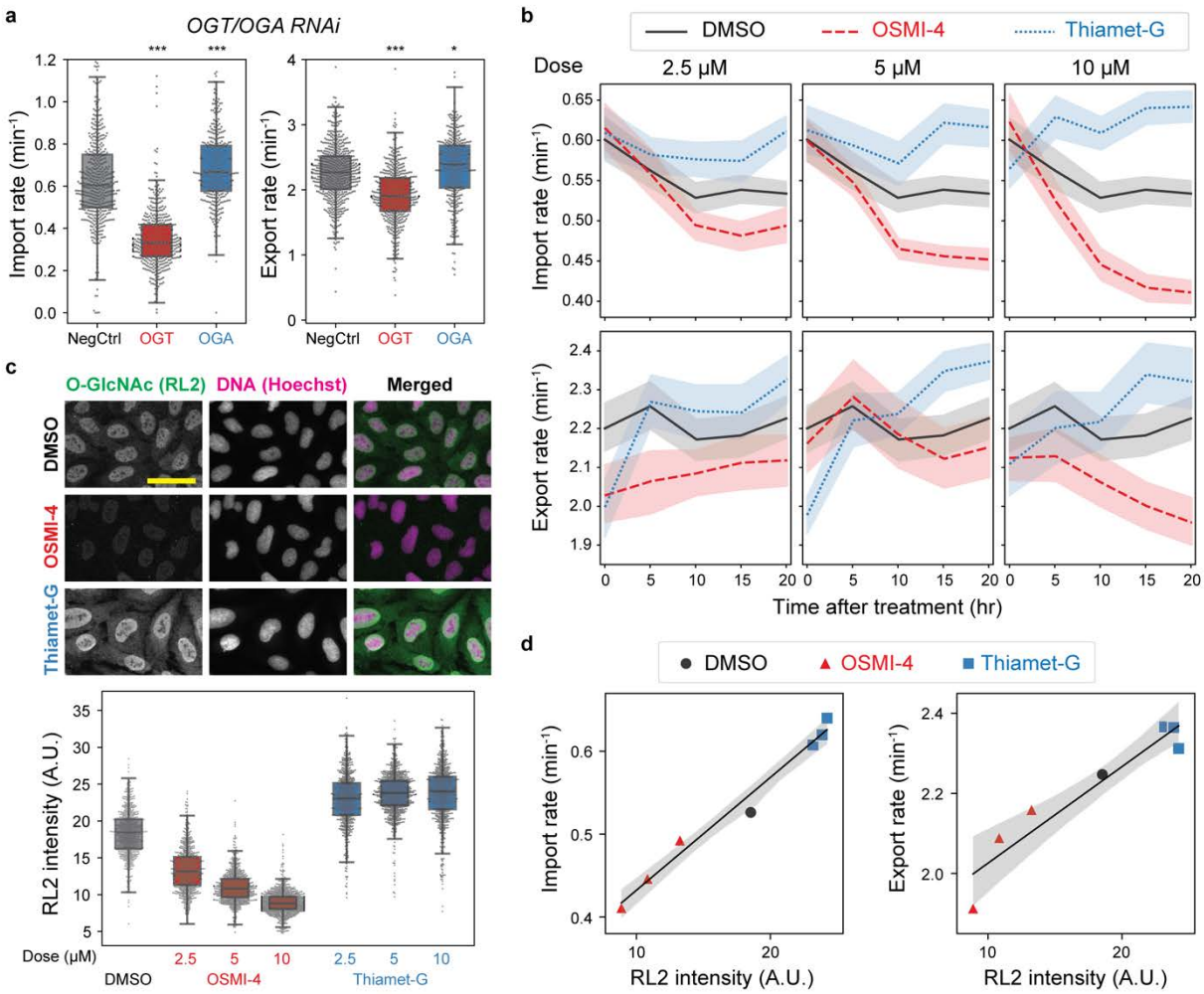

Fig. 2. The nuclear transport rates are dependent on the O-GlcNAc level. a, Nuclear import (left) and export (right) rates after 3 days of transfection with scrambled (NegCtrl), OGT or OGA siRNAs. N>360 nuclei per condition. **b**, Import (top) and export (bottom) rate vs time after treatment with DMSO (black, solid), OSMI-4 (red, dashed) and Thiamet-G (blue, dotted) at 2.5 μM (left), 5 μM (middle), and 10 μM (right). Line and shaded area indicate mean and 95% confidence interval, respectively. N≥120 nuclei per time point per condition. **c**, After the live-cell transport assay in the presence of drugs (shown in **b**), cells were fixed and stained with anti-O-GlcNAc (RL2) antibody and Hoechst 33258. Representative immunofluorescence images of cells treated with DMSO (top), 10 μM OSMI-4 (middle) and 10 μM Thiamet-G (bottom). Scale bar 50 μm. Quantification of nuclear RL2 intensity (background corrected) shown in the plot below the images. N>700 nuclei per condition. **d**, Median import (left) or export (right) rate (from **b**) vs median nuclear RL2 intensity (from **c**), measured after 20-hour treatment with DMSO (black circle), OSMI-4 (red triangle) or Thiamet-G (blue square) at three different doses. Black line and gray shade are the line fit and its 95% confidence interval. p-values were calculated by Welch's t-test for comparison with negative control. n.s.: p>0.01; *: p<1e-2, **: p<1e-3, ***: p<1e-4. The transport assay results are also shown in Extended Data Table 1.

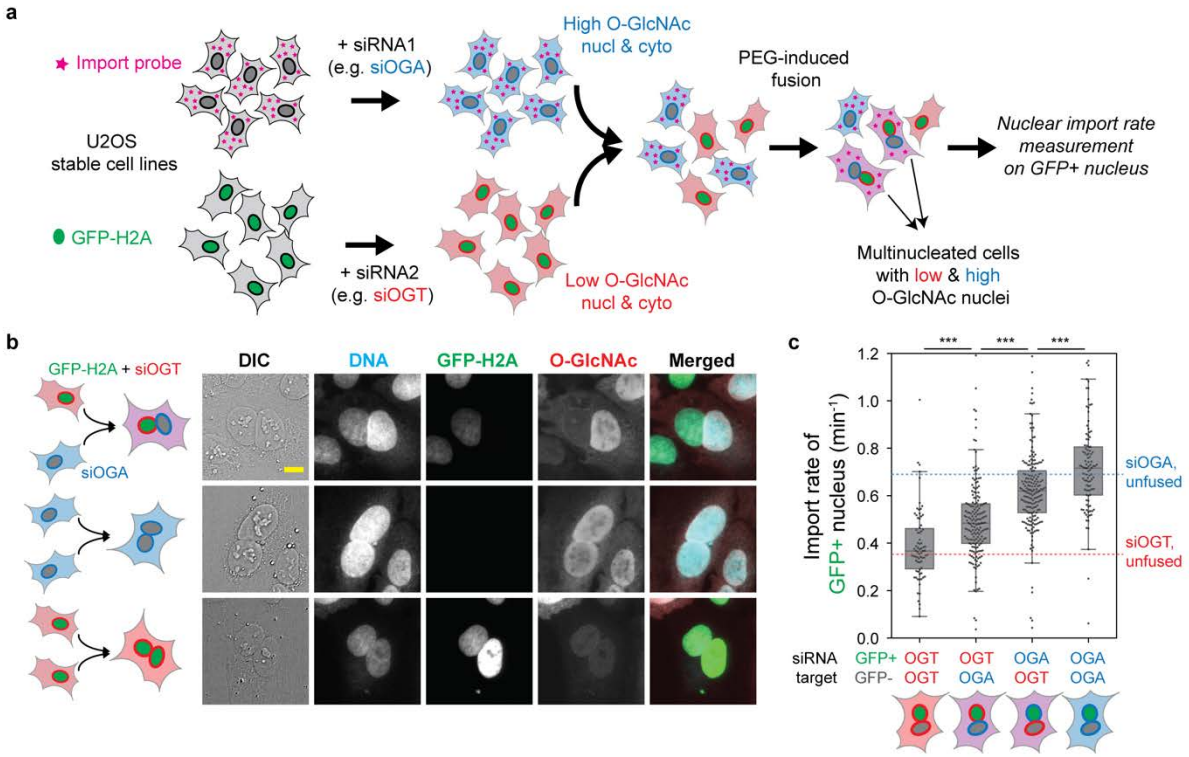

Fig. 3. Heterokaryon analysis reveals that nucleus-confined factors are responsible for the O-GlcNAc dependency of nuclear transport kinetics. a, Schematics of heterokaryon analysis. Two U2OS stable cell lines, one expressing the NES-mCherry-LINuS import probe and the other expressing GFP-H2A, are separately transfected with OGA- or OGT-targeting siRNA, co-cultured, and then fused by brief treatment with PEG. The nuclear import rate was measured on the GFP-positive nuclei in the mCherry-positive fused cells. **b**, RL2 immunofluorescence images of the fused cells, showing that the nuclei largely retains the pre-fusion O-GlcNAc level. 10 μm scale bar. **c**, The nuclear import rate of the GFP+ nucleus in four different fusions (from left to right): GFP-H2A^{siOGT}+import probe^{siOGT}, GFP-H2A^{siOGT}+import probe^{siOGA}, GFP-H2A^{siOGA}+import probe^{siOGT}, and GFP-H2A^{siOGA}+import probe^{siOGA}. Blue and red dotted lines indicate the median nuclear import rates of the unfused cells transfected with siOGA and siOGT, respectively (from Fig. 2a). N≥75 nuclei for each condition. p-values calculated by Welch's t-test where n.s.: p>0.01; *: p<1e-2, **: p<1e-3, ***: p<1e-4.

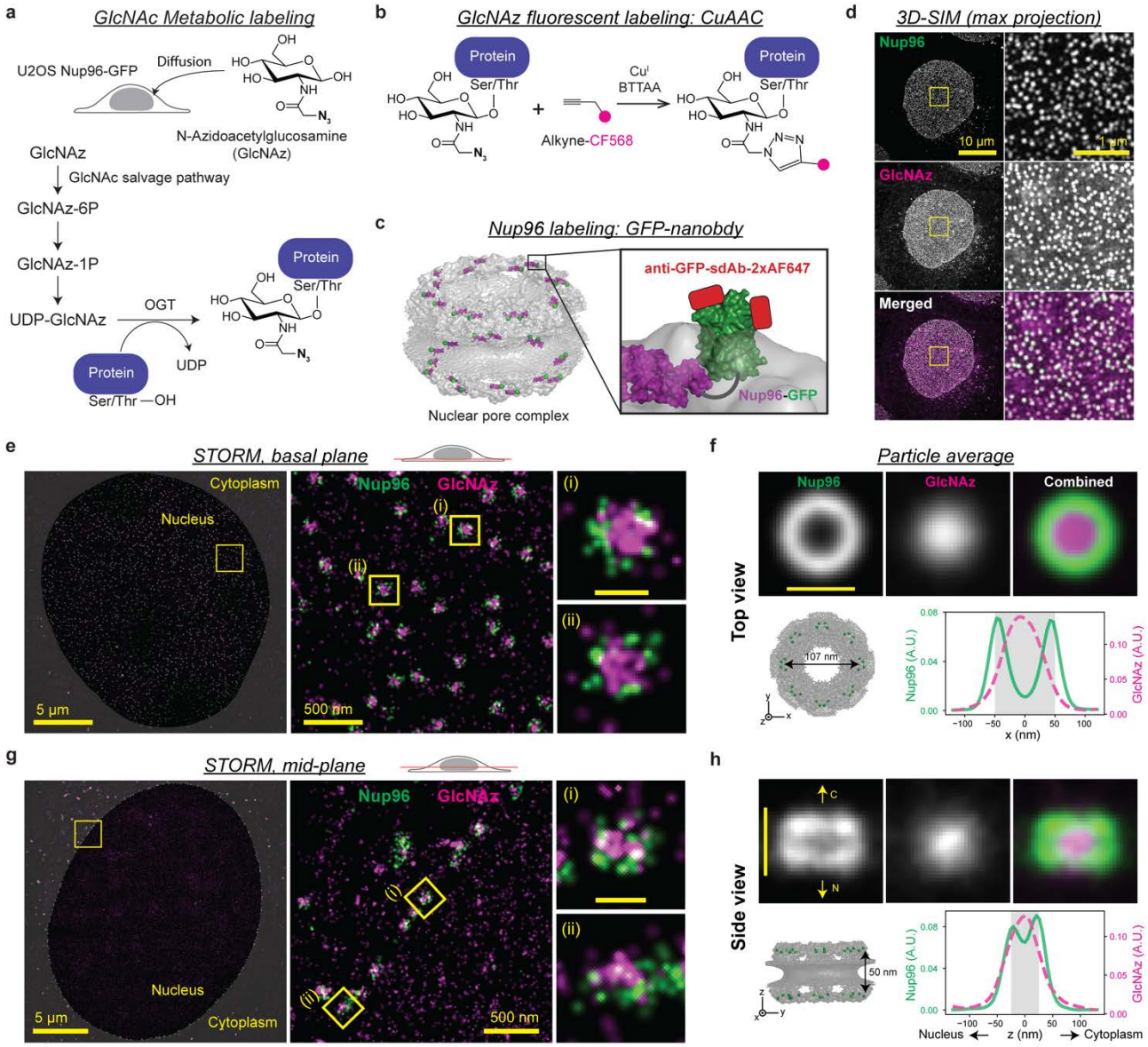

Fig. 4. O-GlcNAc is highly abundant at the central transport channel of the symmetric core of the NPC. a-c, *In situ* fluorescent labeling of Nup96 and O-GlcNAc sites in U2OS cell. **a**, Metabolic labeling of O-GlcNAc site. GlcNAz diffused into the cells is incorporated into proteins via GlcNAc salvage pathway and OGT activity. **b**, The incorporated GlcNAz moieties were labeled with CF568 via copper(I)-catalyzed azide-alkyne cycloaddition (CuAAC). **c**, Nup96 (purple) was endogenously tagged with GFP (green) at the C-terminus. After fixation, each GFP molecule was labeled with up to two anti-GFP single-domain antibodies conjugated with two Alexa Fluor 647 (AF647) (red). **d**, Maximum-intensity projection of 3D-SIM image of the double-stained cells. Left column: full field of view; right column: enlarged region of interest (yellow square). **e and g**, Representative two-color STORM images of the basal plane (in **e**) and mid-plane (in **g**) of the nucleus showing the top and side views of the NPCs, respectively. Each localization of molecules is rendered as a normalized gaussian whose standard deviation is set to the localization precision. **f and h**, Top: averaged top (in **f**) or side view (in **h**) STORM image of the NPCs (703 top views from 4 cells; 122 side views from 4 cells). Bottom left: structure (PDB 5A9Q) of the NPC symmetric core, where the C-terminus of Nup96 is marked with a green sphere. Bottom right: averaged intensity profiles of Nup96-GFP:AF647 (green, solid) and GlcNAz:CF568 (magenta, dashed) along the x- (in **f**) or z-axis (in **h**). Nup98-GFP:AF647 is colored in green and GlcNAz:CF568 in magenta in all merged 3D-SIM and STORM images in **d-h**. Scale bars in individual and averaged pore images in **e-h** are 100 nm.

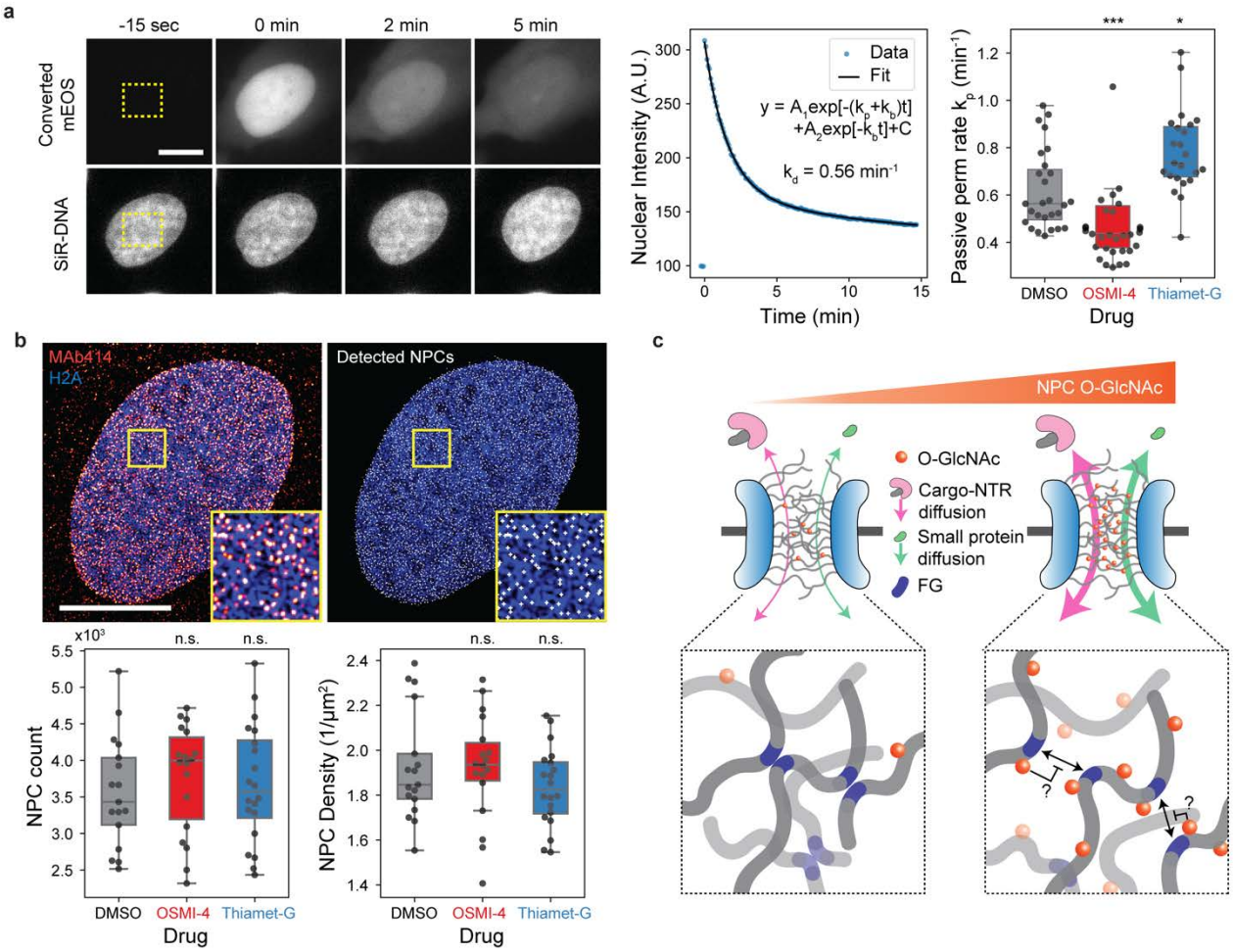

Fig. 5. O-GlcNAcylation enhances the permeability of the NPC. a, Passive diffusion rate measurement. Left representative images: mEOS (top row) in the rectangular region (yellow box) inside the nucleus was selectively converted and continually imaged along with DNA (bottom row). Middle plot: A bi-exponential decay model was fitted to the nuclear intensity of converted mEOS to measure the passive permeation rate k_p. Right box plot: passive permeation rates for cells treated with DMSO, OSMI-4 or Thiamet-G (10 μM, 24 hour). N≥23 cells for each condition. **b,** NPC counting. Top images: 3D-SIM image of MAb414 immunostaining (red) and Halo-H2A:JF646 (blue) and identified NPCs (white). Bottom boxplots: total number (left) and area density (right) of NPCs in cells treated with DMSO, OSMI-4 or Thiamet-G (10 μM, 24 hour). N≥17 cells for each condition. 10 μm scale bars. n.s.: p>0.01; *: p<1e-2, **: p<1e-3, ***: p<1e-4. **c,** Proposed model for O-GlcNAc-dependent modulation of nuclear transport kinetics. Hydrophilic, bulky O-GlcNAc modifications hinder the cohesive interaction between FG repeats, thereby facilitating both passive and NTR-facilitated permeations of molecules through the NPC in both directions.